The surface magnetic activity of the weak-line T Tauri stars TWA 7 and TWA 25

B. A. Nicholson [ID],[1,2]★ G. Hussain,[3,4,5] J.-F. Donati [ID],[5] D. Wright,[2] C. P. Folsom [ID],[5,6] R. Wittenmyer,[2] J. Okumura,[2] B. D. Carter [ID][2] and the MaTYSSE collaboration

[1]*Sub-department of Astrophysics, University of Oxford, Keble Rd, OX1 3RH Oxford, UK*
[2]*University of Southern Queensland, Centre for Astrophysics, 4350 Toowoomba, Australia*
[3]*European Southern Observatory, Karl Schwarzschild Str. 2, D-85748 Garching, Germany*
[4]*Science Division, Directorate of Science, European Space Research and Technology Centre (ESA/ESTEC), Keplerlaan 1, NL-2201AZ Noordwijk, the Netherlands*
[5]*IRAP, Université de Toulouse, CNRS, UPS, CNES, F-31400 Toulouse, France*
[6]*Department of Physics & Space Science, Royal Military College of Canada, PO Box 17000 Station Forces, Kingston ON K7K 0C6, Canada*

ABSTRACT

We present an analysis of spectropolarimetric observations of the low-mass weak-line T Tauri stars TWA 25 and TWA 7. The large-scale surface magnetic fields have been reconstructed for both stars using the technique of Zeeman Doppler imaging. Our surface maps reveal predominantly toroidal and non-axisymmetric fields for both stars. These maps reinforce the wide range of surface magnetic fields that have been recovered, particularly in pre-main sequence stars that have stopped accreting from the (now depleted) central regions of their discs. We reconstruct the large scale surface brightness distributions for both stars, and use these reconstructions to filter out the activity-induced radial velocity jitter, reducing the RMS of the radial velocity variations from 495 to 32 m s^{-1} for TWA 25, and from 127 to 36 m s^{-1} for TWA 7, ruling out the presence of close-in giant planets for both stars. The TWA 7 radial velocities provide an example of a case where the activity-induced radial velocity variations mimic a Keplerian signal that is uncorrelated with the spectral activity indices. This shows the usefulness of longitudinal magnetic field measurements in identifying activity-induced radial velocity variations.

Key words: magnetic fields – techniques: polarimetric – stars: formation – stars: imaging – stars: individual: TWA 7 – stars: individual: TWA 25.

1 INTRODUCTION

Magnetic fields play a key role in the evolution of low-mass stars on to the pre-main sequence (PMS), particularly during the T Tauri stage of cool star evolution. The T Tauri stage is divided into two major categories: classical T Tauri stars (cTTSs) and weak-line T Tauri stars (wTTSs). The cTTS stage starts when the central star has emerged from the cocoon of gas in which it formed, and is surrounded by a substantial disc of gas and dust, from which matter is accreted on to the stellar surface. At this time, magnetic fields are thought to help dissipate the angular momentum of the star and accreting matter such that the stellar rotation does not reach break-up speed as the star forms. Once the gas from the inner disc is cleared and accretion on to the star has ceased, the star is then classed as a wTTS; a fully formed star that is still undergoing contraction towards its main-sequence size, often still surrounded by an extended debris disc.

The study of the differences between these populations of PMS stars has been one of the goals of the Magnetic Topologies of Young Stars and Survival of close in Giant Exoplanets (MaTYSSE) large program. MaTYSSE is a multitelescope programme using high-resolution spectropolarimetric observations to map the large-scale brightness and magnetic fields of a range of wTTSs, and compare them to a sample of cTTSs observed in the Magnetic Protostars and Planets[1] (MaPP) programme (see e.g. Donati et al. 2007, 2008; Hussain et al. 2009; Donati et al. 2010, 2011, 2012).

Few stars below ∼0.8 M$_\odot$ have been observed in either sample, as their peak emission in the infrared and low brightness make them challenging targets for current optical spectropolarimeters. Within the MaPP sample, there have been 3 PMS stars below this limit [when compared with the Baraffe et al. (2015) PMS evolution models], DN Tau (0.65 M$_\odot$; Donati et al. 2013), BP Tau (0.7 M$_\odot$; Donati et al. 2008), and V2247 Oph (0.35 M$_\odot$; Donati et al. 2010), and two stars with masses around 0.8 M$_\odot$, TW Hya (Donati et al. 2011) and AA Tau (Donati et al. 2010). The magnetic field of V2247 Oph appeared significantly different compared to the other stars' magnetic field. The star is fully convective like its higher mass counterparts of the same age, but displayed a wildly different magnetic field morphology.

To further our understanding of low-mass PMS dynamo fields, this work presents an analysis of high-resolution spectropolarimetric data of two low-mass wTTS stars as part of the MaTYSSE sample: TWA

---

[1]https://wiki.lam.fr/mapp/FrontPage

25 and TWA 7. Both are 10 Myr old stars in the TW Hya association (Mentuch et al. 2008), and represent more evolved versions of the MaPP stars AA Tau (in the case of TWA 25), and DN Tau (in the case of TWA 7).

In this analysis, we reconstruct the surface brightness and large-scale magnetic field morphologies of both stars. In addition, we examine the variation in longitudinal (line of sight) magnetic field with stellar rotation, as well as the spectral activity markers of H α and Na I doublet indices.

The other major focus of the MaTYSSE program is the search for close-in giant planets around wTTSs. Finding planets around very active stars is challenging, as the surface activity of these stars can contribute to radial velocity variations of the order of hundreds of meters per second, obscuring even a giant planet's signal. The MaTYSSE program has addressed this by using the surface activity information provided from surface brightness mapping to measure and remove the radial velocity contribution due to this activity (Donati et al. 2014). This work, therefore, also analyses the radial velocities of TWA 25 and TWA 7, and uses the surface brightness information from our Doppler mapping to filter out activity jitter from the radial velocities of both stars.

In Section 2, we detail the observations and data processing of TWA 25 and 7. The evolutionary states of both stars are determined, and the stellar properties calculated in Section 3. Section 4 describes the mapping of large-scale brightness and magnetic fields, Section 5 explores the rotational modulation of the longitudinal magnetic field and activity indices, and Section 6 describes our analysis of the radial velocities for both stars. Lastly, we summarize and discuss our findings in Section 7.

2 OBSERVATIONS

High-resolution spectropolarimetric data were taken for TWA 25 and TWA 7, using HARPS in polarimetric mode on the ESO 3.6-m telescope in La Silla, Chile. TWA 25 was observed 16 times and TWA 7 observed 17 times from 2017 March 12–31. Journals of the observations for each star are given in Tables 1 and 2. Each observation consists of four sub-exposures with alternating configurations of a quarter wave plate to remove first-order spurious polarization signals. Two observations of TWA 7 contain only two sub-exposures due to weather, and so are only used for the analysis involving brightness information, and are excluded from the magnetic field analysis. Our spectra have a wavelength coverage of ∼380 to ∼690 nm, and spectral resolution of ∼115 000. The spectral data were reduced using the LIBRE ESPRIT pipeline software adapted for use with HARPS polarimetric data (Hébrard et al. 2016), following the procedure outlined in Donati et al. (1997). Across our observations we attain a peak circular polarization (Stokes V) signal-to-noise ratio (SNR) of between 72 and 119 for TWA 25, with a median value of 95, and between 55 and 110 for TWA 7, with a median value of 92.

2.1 Least squares deconvolution

To increase the signal-to-noise ratio for our tomographic mapping, we combine the lines in our observed spectra using Least Squares Deconvolution (LSD; Donati et al. 1997). This process combines the signal in absorption features, by deconvolving our observed spectra with a mask of photospheric lines constructed using the Vienna Atomic Line Database (VALD3; Ryabchikova et al. 2015) based on the effective temperature and surface gravity of each star (see Section 3), and removing lines in emission, or with broad absorption.

Given the large number of weak and blended absorption lines at the spectral types of these stars, we remove lines with a strength relative to the deepest lines of less than 0.1, as per Nicholson et al. (2018) to limit the effect of blends. After generating these LSD profiles, the continuum levels were re-normalized, and all were scaled by the mean equivalent width for each star using the re-normalization program within the ZDIPY package (Folsom et al. 2018). The Stokes I and Stokes V LSD profiles are plotted as black lines in Figs 1 and 2 for TWA 25, and Figs 3 and 4 for TWA 7. For TWA 25, the peak SNR in the intensity spectra increase from 123 to 656 in the Stokes I LSD profiles, and in the circular polarisation spectra the peak SNR increased from 119 to 4838 in the Stokes V LSD profiles. For TWA 7, we obtain an increase in peak SNR of our intensity spectra from 111 to 404 in the LSD profiles, and in the circular polarization spectra we get an increase from 110 to 3993 in the Stokes V LSD profiles.

3 STELLAR PARAMETERS OF TWA 25 AND TWA 7

TWA 25 and TWA 7 are both single stars in the TW Hya association (Song, Zuckerman & Bessell 2003; Webb et al. 1999), which has a mean age of 10 Myr (Mentuch et al. 2008). To estimate the individual ages, and hence the evolutionary states for each star, we estimate their effective temperatures and surface gravities from observations, and calculate bolometric luminosities based on properties of the stars found in the literature. A summary of the stellar parameters discussed in this section and used for our analysis is given in Table 3.

3.1 Effective temperature and surface gravity

We calculate the effective temperature ($T_{\rm eff}$) and logarithmic surface gravity (log (g)) for both stars using the HARPS observations presented here, following the method outlined in Donati et al. (2012), which is based on the procedure of Valenti & Fischer (2005). This method determines effective temperatures and surface gravities by comparing select atomic absorption regions in high resolution optical spectra to a grid of template synthetic spectra. For TWA 25 we find an $T_{\rm eff}$ = 4120 ± 50 K and log (g) = 4.3 ± 0.1, and for TWA 7 we find $T_{\rm eff}$ = 3800 ± 50 K and log (g) = 4.7 ± 0.2. The larger uncertainty on log (g) for TWA 7 is due to the solution being at the edge of the model grid.

There are many $T_{\rm eff}$ values for TWA 25 and TWA 7 within the literature, ranging from 3742 (da Silva et al. 2009) to 4250 K (Ammons et al. 2006) for TWA 25, and from 3300 (Yang, Johns-Krull & Valenti 2008) to 4017 K (Gaia Collaboration et al. 2018) for TWA 7. Such a wide range in effective temperatures is unsurprising for pre-main sequence stars, and is likely due to the differences in methods used and the relative sensitivity of those methods to the presence of photospheric spots. For example, both Ammons et al. (2006) and Gaia Collaboration et al. (2018) are large surveys, performing the same temperature analysis across their whole sample. Such a broadbrush approach is typically not appropriate for PMS stars due to their atypical nature.

Mentuch et al. (2008) perform a detailed spectral analysis consistently for both stars, determining both $T_{\rm eff}$ and log (g) values, as is needed for pre-main sequence stars. Mentuch et al. analyse high-resolution spectra of both stars using select atomic and molecular absorption regions, and find effective temperatures and logarithmic surface gravities of 3920 ± 150 and 4.45 ± 0.5 for TWA 25, and 3540 ± 150 and 4.18 ± 0.5 for TWA 7. Whilst the surface gravity estimates are in agreement within the uncertainties, the effective temperatures differ by more than 1σ of either estimate.

Table 1. Journal of observations for star TWA 25. From left to right: This table lists the date of observation, the Heliocentric Julian date, the exposure time as a set of sub-exposures, the stellar rotational phase based on a period of 5.07 d (with the zero-point set as the middle of the first observation), the peak SNR in the Stokes I and V spectra per observation, and the SNR in Stokes I and V after least squares deconvolution (LSD; see Section 2.1). The final column gives the status of magnetic field detection based on False Alarm Probably (FAP) values, with definite detection (D) for FAP $< 10^{-5}$, marginal detection (M) for $10^{-5} <$ FAP $< 10^{-3}$, and non-detection (N) for FAP $> 10^{-3}$.

Date (2017)	HJD (2457000+)	Exposure time (s)	Rotation cycle	Stokes I Spec. SNR	Stokes V Spec. SNR	Stokes I LSD SNR	Stokes V LSD SNR	Detection Status
March 12	825.83150	4 × 1600	0.00	107	103	637	4381	D
March 13	826.82463	4 × 1600	0.20	78	74	617	2907	D
March 16	829.80554	4 × 1600	0.78	120	116	653	4809	D
March 17	830.83104	4 × 1600	0.99	99	92	635	3812	D
March 18	831.81629	4 × 1600	1.18	108	102	618	4088	D
March 20	833.81797	4 × 1600	1.58	84	83	654	3304	D
March 21	834.86501	4 × 1600	1.78	113	111	653	4424	D
March 22	835.86077	4 × 1600	1.98	99	95	633	3727	D
March 23	836.82937	4 × 1600	2.17	93	91	616	3494	D
March 24	837.82846	4 × 1600	2.37	91	88	627	3433	D
March 25	838.82821	4 × 1600	2.56	93	91	642	3583	D
March 26	839.82925	4 × 1600	2.76	123	119	651	4838	D
March 27	840.83804	4 × 1600	2.96	100	95	639	3832	D
March 28	841.82974	4 × 1600	3.16	75	72	607	2779	D
March 30	843.82681	4 × 1600	3.55	108	104	640	4203	D
March 31	844.83717	4 × 1600	3.75	109	105	656	4241	D

Table 2. Table of observations for star TWA 7. For description, see caption of Table 1. Rotation cycle is calculated based on a 5.00 d period. The observations on the March 18 and 19 were incomplete due to weather, and so are excluded from the magnetic field analysis.

Date (2017)	HJD (2457000+)	Exposure Time (s)	Rotation Cycle	Stokes I Spec. SNR	Stokes V Spec. SNR	Stokes I LSD SNR	Stokes V LSD SNR	Detection Status
March 12	825.75835	4 × 1300	0.00	74	73	396	2450	N
March 13	826.74890	4 × 1500	0.20	75	71	392	2535	N
March 16	829.69035	4 × 1600	0.79	111	110	382	3945	D
March 17	830.75377	4 × 1600	1.00	96	92	393	3279	N
March 18	831.72533	2 × 1600	1.19	75	72	404	2665	–
March 19	832.72506	2 × 1600	1.39	55	55	360	2060	–
March 21	834.78337	4 × 1650	1.80	86	82	390	2877	D
March 22	835.78202	4 × 1650	2.00	75	71	391	2468	N
March 23	836.74918	4 × 1750	2.20	90	87	388	3044	M
March 24	837.74774	4 × 1750	2.40	107	101	389	3727	D
March 25	838.53731	4 × 1750	2.56	111	106	391	3993	D
March 25	838.74812	4 × 1750	2.60	97	92	382	3296	D
March 26	839.74884	4 × 1750	2.80	106	101	376	3600	D
March 27	840.75775	4 × 1750	3.00	101	98	372	3410	N
March 28	841.74953	4 × 1750	3.20	78	74	381	2612	M
March 30	843.74606	4 × 1750	3.60	103	101	386	3593	M
March 31	844.75641	4 × 1750	3.80	105	105	386	3622	D

This discrepancy in effective temperature estimate is likely due to the inclusion of molecular absorption regions, which will give a systematically lower temperature due to those lines also being present in cool spots on the stellar surface. This is also the likely explanation for the lower temperature estimates of da Silva et al. (2009) for TWA25 and Yang et al. (2008) for TWA 7.

3.2 Luminosity

Luminosity is calculated for both stars based on their apparent magnitudes, extinction estimates, bolometric corrections, and distances. For TWA 25, we use an apparent V magnitude of 11.160 ± 0.083 mag from Henden et al. (2015), and a bolometric correction of -0.97 ± 0.05 mag from Pecaut & Mamajek (2013). Interstellar extinction, A_v, is calculated using the observed B-V colour of

1.428 ± 0.162 mag from Henden et al. (2015) and intrinsic colour, $(B - V)_0$, of 1.18 ± 0.03 mag from Pecaut & Mamajek (2013), giving $A_v = 0.8 \pm 0.5$ mag for TWA 25. The distance to TWA 25 is calculated as 53.1 ± 0.2 pc from parallax measurements from *Gaia* Data Release 2 (DR2; Gaia Collaboration et al. 2016, 2018). These values result in a luminosity of $0.4^{+0.2}_{-0.1}$ L$_\odot$ for TWA 25. This value is higher than any previously published values, though the large uncertainty means that it is consistent with literature values. Our luminosity value is in closest agreement with the value of 0.252 L$_\odot$ published by McDonald, Zijlstra & Watson (2017), who estimate an even higher extinction value of 0.643 mag, but use a smaller distance derived from the first *Gaia* data release. The extinction values for TWA 25 are all calculated (here and in the literature) as greater than zero despite its close proximity (making significant interstellar extinction unlikely), indicating reddening due to spots on the stellar surface.
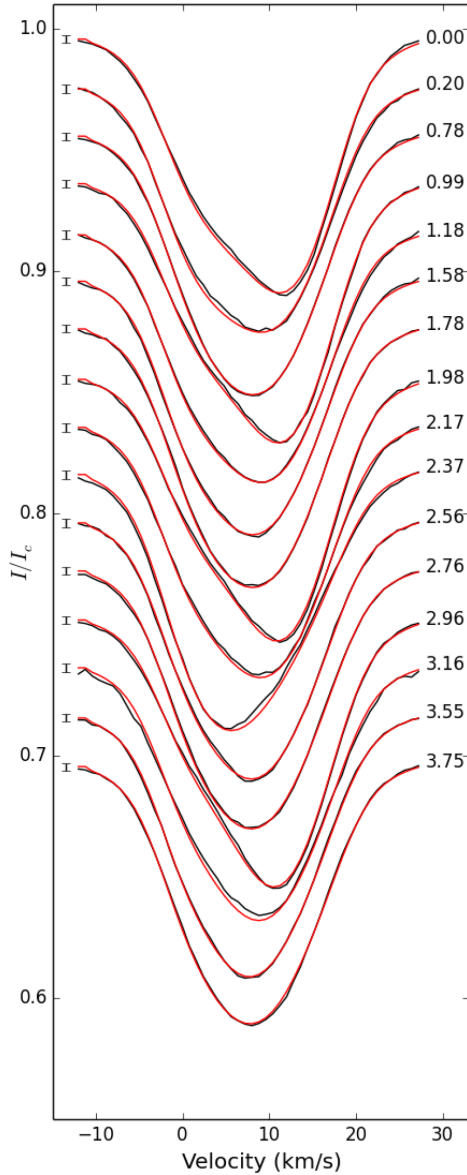
Figure 1. Stokes I LSD profiles (black line) of TWA 25, and fits to these profiles using DOTS (red line, see Section 4.1). Mean 1σ error bars are given to the left of each profile, and rotation phase is given on the right.
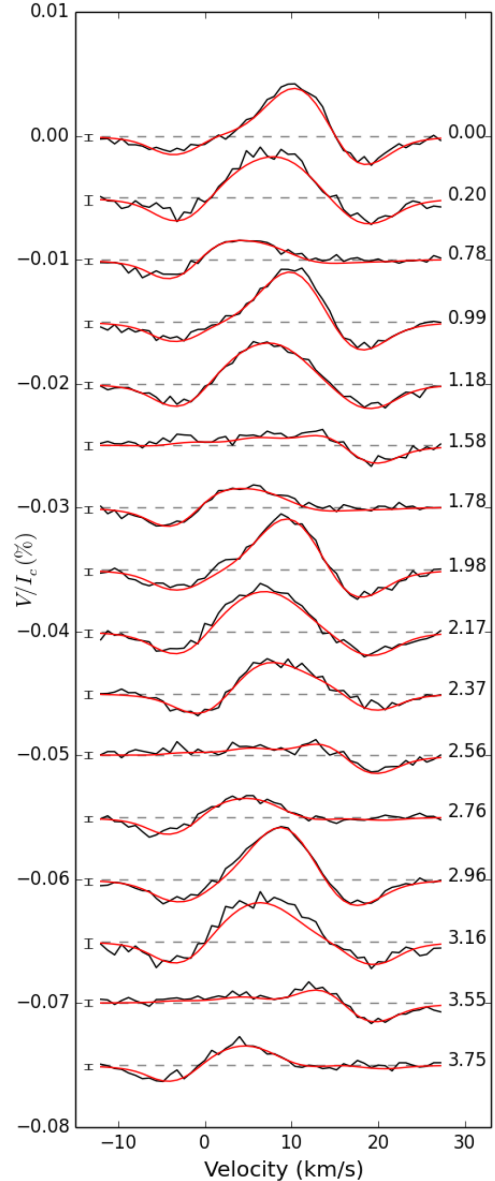

Figure 2. Circular polarization (Stokes V) LSD profiles for TWA 25 (black line), with fits from Zeeman Doppler Imaging (red line, see Section 4.2). Mean error bars for each observation are shown on the left-hand side, and rotation phase of each observation is given on the right-hand side.

To calculate the luminosity of TWA 7, we use an apparent V magnitude of 11.754 ± 0.57 mag from Henden et al. (2015), and a bolometric correction of -1.34 ± 0.08 mag from Pecaut & Mamajek (2013). We calculate A_v using observed $B - V$ colour of 1.475 ± 0.063 mag from Henden et al. (2015) and $(B - V)_0$ of 1.37 ± 0.02 from Pecaut & Mamajek (2013), giving $A_v = 0.2 \pm 0.2$ mag for TWA 7. Our estimate of extinction, given its large uncertainties, is equivalent to the usual assumed extinction of zero for this star. The *Gaia* DR2 parallax measurement of TWA 7 gives a distance of 34.03 ± 0.08 pc. These values result in a luminosity of 0.08 ± 0.02 L$_\odot$ for TWA 7. This value is also in good agreement with all literature values, with the exception of a very high estimate of 0.32 L$_\odot$ by Low et al. (2005), who calculate a stellar luminosity by integrating a spectral energy distribution constructed from *Spitzer* data, assuming an averaged distance to TWA of 55 pc. Scaling this luminosity value to the updated Gaia Collaboration et al. (2018)

distance of 34.03 pc, we get a luminosity estimate of $\sim$0.12 L$_\odot$, which is in better agreement with the other values in the literature.

Both stars are expected to have heavily spotted photospheres that influence their observed colours and visual magnitudes, and in turn their luminosity estimates. Given stellar evolution models do not account for spotted photospheres, we apply a first-order spot correction to our luminosity values to make better estimates of the stars' evolutionary states. Following the method of Yu et al. (2019), we assume $A_v = 0$ (a reasonable assumption for stars this close) and an average spot coverage of 50 ± 15 per cent, chosen as a conservative estimate based on the finding of total spot coverage of V140 Tau ($50 - 75$ per cent Yu et al. 2019) and LkCa 4 ($\sim$80 per cent Gully-Santiago et al. 2017). Although our tomographic mapping results (see Section 4.1) give a smaller percentage spot coverage, DI is not sensitive to the small scale spot features that contribute to the
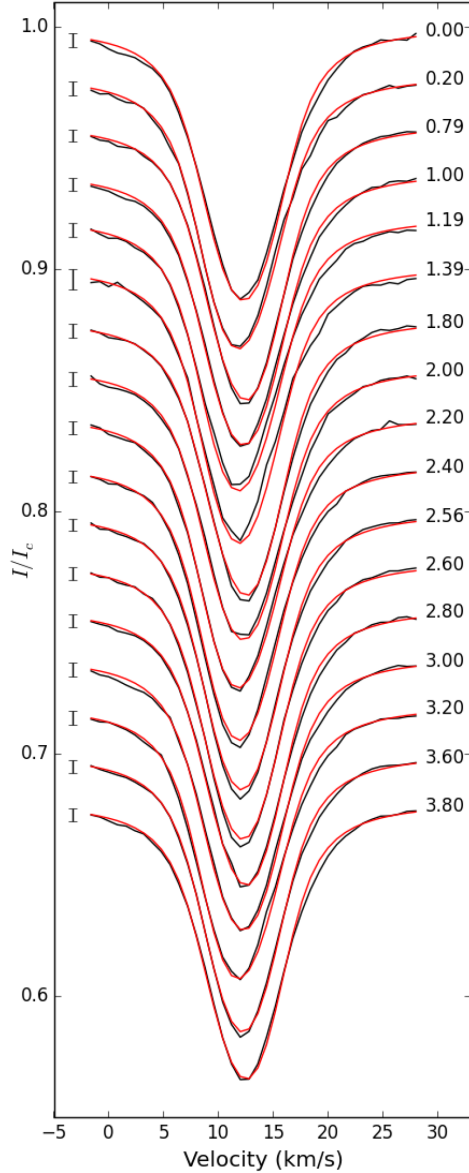
Figure 3. Stokes I LSD profiles (black line) of TWA 7, and fits to these profiles using DOTS (red line, see Section 4.1). Mean 1σ error bars are given on the left-hand side of each profile, and rotation phase is given on the right.
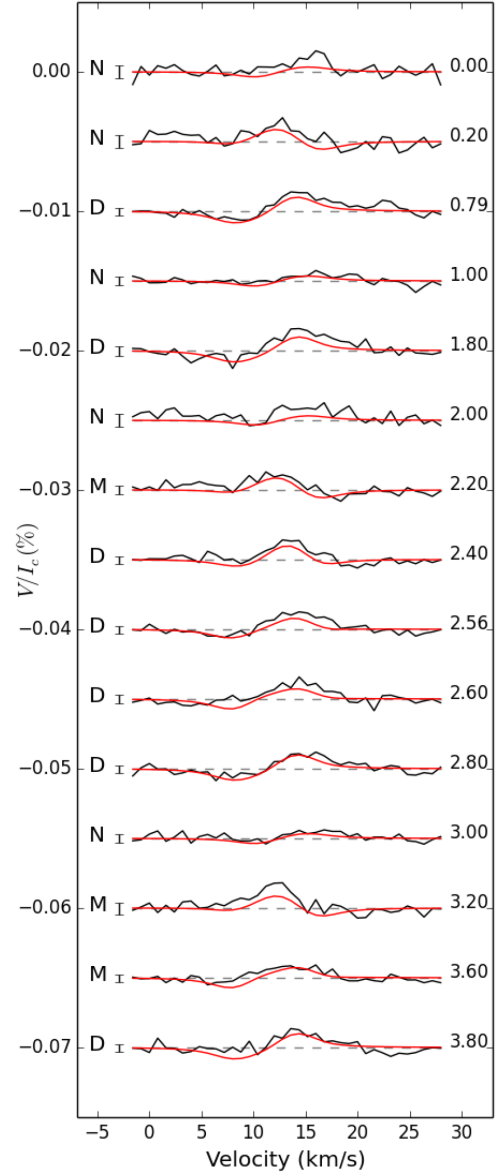
Figure 4. Circular polarization (Stokes V) LSD profiles for TWA 7 (black line), with fits from Zeeman Doppler Imaging (red line, see Section 4.2). On the left-hand side of each profile is the mean error bar, and a letter denoting the level of magnetic signal detection for each observation are shown on the left-hand side, and rotation phase of each observation is given on the right-hand side. The observations taken on March 18 and 19 were incomplete and are not shown in this plot, as they are excluded from the magnetic field analysis.

reddening, and thus underestimate the total area of spot coverage. With this assumed extinction and spot coverage values, we obtain a spot-adjusted luminosity of 0.4 ± 0.1 L$_\odot$ for TWA 25 and $0.12^{+0.04}_{-0.03}$ L$_\odot$ for TWA 7.

3.3 Masses, radii, ages, and evolutionary stages

Using our calculated luminosities and effective temperatures, we calculate mass, age, and stellar radius for both stars based on the Baraffe et al. (2015) pre-main sequence stellar evolution models. The locations of TWA 25 and TWA 7 on the HR diagram with respect to these mass tracks and isochrones are shown in Fig. 5. Stellar masses, radii, and ages derived for both stars are given in Table 3. The age estimate for both stars are in agreement within 1σ with the average age of 10 Myr for the TW Hya Association (Mentuch et al. 2008).

Table 3. Summary of the calculated properties of TWA 25 and 7.

	TWA 25	TWA 7
Mass, M_* (M$_\odot$)	$0.83^{+0.04}_{-0.06}$	0.62 ± 0.03
Radius, R_* (R$_\odot$)	1.2 ± 0.2	$0.8^{+0.2}_{-0.1}$
Age (Myrs)	7^{+7}_{-4}	17^{+19}_{-9}
Luminosity, L_* (L$_\odot$)	0.4 ± 0.1	$0.13^{+0.05}_{-0.03}$
Distance, (pc)	53.1 ± 0.2	34.03 ± 0.08
$v\sin(i)$ (km s^{-1})	11.9 ± 0.3	4.5 ± 0.2
Rotation period, $P_{\rm rot}$ (d)	5.07 ± 0.03	5.00 ± 0.01
Effective temperature, $T_{\rm eff}$ (K)	4120 ± 50	3800 ± 50
Surface gravity, log (g)	4.25 ± 0.1	4.7 ± 0.2
Inclination angle, i (Deg)	57 ± 5	40^{+5}_{-15}

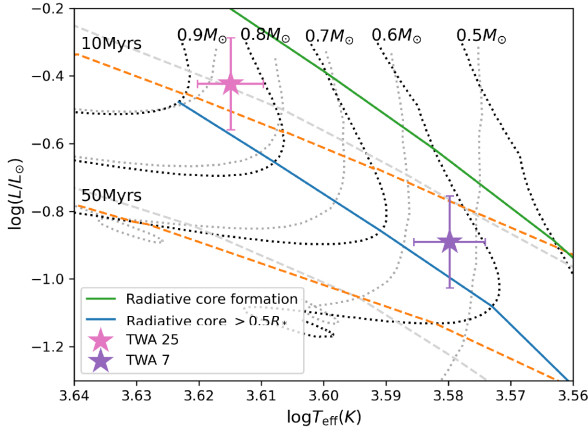**Figure 5.** HR diagram showing the locations, including 1σ uncertainties, of TWA 25 (pink) and TWA 7 (purple) with relation to the Baraffe et al. (2015) PMS evolutionary models. The black dotted lines are evolutionary tracks for 0.9 $M_\odot$, 0.8 $M_\odot$, 0.7 $M_\odot$, 0.6 $M_\odot$, and 0.5 $M_\odot$, the orange dashed lines are the 10Myr and 50 Myr isochrones, the solid green line indicates the boundary between full convection and the formation of a radiative core, and the solid blue line shows the point at which that radiative core is greater than half the stellar radius. The grey dotted and dashes lines are the corresponding mass tracks and isochrones from the Siess, Dufour & Forestini (2000) evolution tracks for comparison.

Investigating the internal structure of these stars, it can be seen in Fig. 5 that these stars sit above the boundary where the radiative core grows to greater than half the stellar radius (solid blue line in), with TWA 25 estimated to have formed a radiative core of size 0.3 ± 0.2 R_*, and TWA 7 is expected to have a radiative core of 0.4 ± 0.2 R_*.

3.4 Inclination

For tomographic mapping, knowing the stellar inclination is crucial for interpreting how the variability in the LSD profiles relates to the latitudes of recovered surface features. It is also one of the more challenging stellar parameters to determine. For TWA 25 and TWA 7, we consider both the estimates of debris disc inclination from imaging studies as a proxy for stellar inclination, and calculate the inclination based on stellar parameters. Choquet et al. (2016) imaged both TWA 25 and TWA 7 with NICMOS on the *Hubble Space Telescope*, and calculate a disc inclination of 75 ± 6 deg for TWA 25 and 22 ± 22 deg for TWA 7, where 0 deg represents a face-on disc (and pole-on star if the disc and stellar rotation axes are aligned). TWA 7 has also been observed by Olofsson et al. (2018) who used SPHERE on ESO's Very Large Telescope, refining TWA 7's disc inclination to $13.1^{+3.1}_{-2.6}$ deg.

To test if these disc inclinations are reasonable approximations for the stellar inclination, we calculated the implied stellar radius given our measured $v\sin(i)$ and $P_{\rm rot}$ values. For TWA 25, we find a theoretical radius of $1.23 \pm 0.05 R_\odot$, which agrees with our estimates from PMS evolution models within a 1σ uncertainty. For TWA 7, however, we find a theoretical radius of $2.0^{+0.5}_{-0.4}$ $R_\odot$ based on the Olofssson et al. inclination estimate. This is far larger than any radius suggested by the PMS models for a star of this temperature and luminosity, and is unlikely given the age of this star and star-forming region. This is also true for radii calculated from inclinations 3σ above the disc inclination estimate. This suggests that the observed disc is misaligned with respect to the stellar rotation axis.

We next calculate the inclination from the measured $v\sin(i)$ and $P_{\rm rot}$ values in our data, and the stellar radius determined from our

bolometric luminosities and the effective temperatures determined above. For TWA 25, we calculate an inclination of 81 ± 63 deg, and for TWA 7 we get an inclination of 32 ± 6 deg. Given the massive uncertainties, especially with the inclination of TWA 25, we leave inclination as a free parameter in our tomographic modelling of both stars for consistency, and it is these inclination values that are given in Table 3.

4 TOMOGRAPHIC MODELLING

4.1 Doppler imaging

Using the Stokes I LSD profiles described in Section 2.1, and the stellar parameters given in Table 3, we reconstruct the surface brightness of TWA 7 and TWA 25 using the technique of Doppler Imaging (DI). For this, we used the DOTS code (Collier Cameron 1997), with modifications to reconstruct areas of both bright plage and cool spot, as described in Donati et al. (2014). This code inverts the Stokes I data and applies a maximum entropy regularization to determine the simplest map that best fits our data. The surface brightness was reconstructed, assuming a Milne–Eddington model atmosphere for the local line profile, and using mean Landé factor of 1.192, mean wavelength of 544 nm (as set by the LSD profiles), and a linear limb darkening coefficient of 0.72. In this process, we fit for the $v\sin(i)$, line equivalent width (EW), radial velocity, rotation period, and inclination for each star. The parameters are determined by pushing to a low value of reduced χ^2 while varying the parameters, except for $v\sin(i)$ and EW, these are done separately. Radial velocity, period, and inclination are fit first and then $v\sin(i)$ and EW are varied on a fine grid and noting the reduced χ^2 values achieved within a set number of iterations (usually 20). The curves around our parameter grids show parabolic shapes for radial velocity, period and $v\sin(i)$ and EW, and so the parameters quoted and the associated uncertainties are determined using parabolic fits to the chi-squared minimization. For TWA 25, we estimate the average radial velocity, rotation period, and $v\sin(i)$ to be 8.33 ± 0.25 km s^{-1}, 5.07 ± 0.03 d, and 11.9 ± 0.3 km s^{-1}, respectively. For TWA 7, we find an average radial velocity of 13.18 ± 0.25 km s^{-1}, rotation period of 5.00 ± 0.01 d and $v\sin(i)$ of 4.5 ± 0.2 km s^{-1}. The inclination grids do not show a parabolic shape so this method could not be used to determine inclinations – the plots show defined minima over a range of inclination angles, which are used as rough estimates of appropriate ranges of stellar inclination for these systems. For TWA 25, this is 57 ± 5 deg and 40^{+5}_{-15} deg for TWA 7. We were unable to detect the presence of differential rotation in the Stokes I data of either star.

Our resulting fits to the Stokes I profiles are shown in red in Figs 1 and 3, and our reconstructed surface brightness maps are shown in Figs 6 and 7. TWA 25 displays large areas of both bright plage and cool spots at high, mid, and low latitudes.

The reconstructed surface brightness maps of TWA 7 show a similar morphology, with one large region of cool spot, a large area of plage. The simplicity of the map is due to the lack of resolution of the stellar surface which results from the star having a low $v\sin(i)$, which in turn limits the spatial resolution of the resulting map.

4.2 Zeeman Doppler imaging

The large-scale surface magnetic fields are reconstructed for each star from their Stokes V LSD profiles using the Zeeman Doppler Imaging (ZDI) program ZDOTS (Hussain et al. 2000, 2002, 2016), which is essentially DOTS applied to circularly polarized spectra. ZDOTS allows the surface magnetic field to be expressed as a series
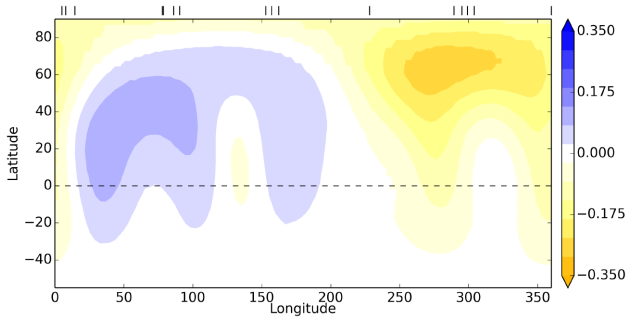
Figure 6. Surface brightness map of TWA 25, showing areas of bright plage (blue, >0), and areas of cool spot (yellow, <0), relative to the photosphere (0.0). The black dashed line indicates the equator, and the top tick marks indicate observed longitudes.
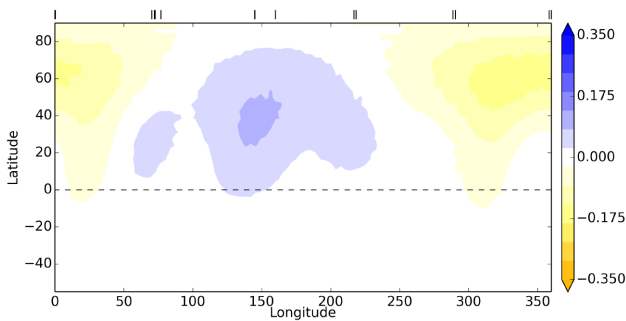

Figure 7. Surface brightness map of TWA 7, showing areas of bright plage (blue, >0), and areas of cool spot (yellow, <0), relative to the photosphere (0.0). The black dashed line indicates the equator, and the top tick marks indicate observed longitudes.

of spherical harmonics, and uses maximum entropy regularization to find the simplest field configuration that best fits our Stokes V LSD profiles. The Stokes V profiles are modelled in a weak field approximation, using a mean Landé factor and central wavelength equivalent to those of the Stokes V LSD profiles. The stellar model, including line profile modelling and stellar parameters are identical in both DOTS and ZDOTS, and we take into account the surface brightness reconstructions produced above in our reconstruction of the stellar surface magnetic field maps.

For TWA 25, the reconstructed radial, azimuthal and meridional components of the large-scale magnetic field are shown in Fig. 8, with the associated fit to the Stokes V profiles shown in Fig. 2. Since it is easy of overfit data in ZDI, an optimum reduced χ^2 was determined using the method of Alvarado-Gómez et al. (2015), resulting in reduced χ^2 of 1.124 for this fit.

In the fitting process, we investigate the presence of differential rotation, and find a best-fitting equatorial rotation period of 5.01 ± 0.03 d, and a shear value of 0.025 ± 0.04 rad d^{-1}. Our reconstructed field has a mean total field strength of 535 G, and shows a far stronger azimuthal field compared to the radial or meridional fields, as well as a high level of non-axisymmetry in the radial component. We quantify this by examining the distribution of energy among the different spherical harmonic components. This solution indicates a dominantly toroidal field (83 per cent energy in toroidal components). The poloidal field is highly non-axisymmetric, with 97 per cent of the poloidal field energy not aligned with the stellar rotation axis, but it is relatively simple, with 80 per cent of the poloidal field contained in the dipolar and quadrupolar components.

The reconstructed large-scale surface magnetic field maps for TWA 7 are shown in Fig. 9, and the fit to the Stokes V LSD profiles are shown in Fig. 4, fit to an optimum reduced χ^2 of 1.21. Given the poorer signal-to-noise ratio (SNR) of these observations, we note in Fig. 4 that profiles are definite magnetic detections, defined as having a false alarm probability (FAP) less than 10^{-5}, a marginal detection with a FAP between 10^{-5} and 10^{-3}, or a non-detection with FAP greater than 10^{-3}. Not included in this figure are observations lacking the full set of four sub-exposures, as these are excluded from the ZDI analysis.

We are unable to obtain information about any surface differential rotation, though we do obtain a best-fitting rotation period of 5.00 ± 0.01 d from a reconstruction using just the Stokes V profiles, which is in agreement with the rotation period determined using just the intensity profiles. The resulting reconstructed large-scale magnetic field has a mean total field strength of 30 G, and, as with TWA 25, show a strong azimuthal band at mid-latitudes. The meridional field is weaker, but this is typically the case with ZDI, due to some degree of cross-talk between the meridional and radial magnetic field components, though this effect is reduced by expressing the field as spherical harmonics (Donati et al. 2001). We again quantify the large-scale by examining the percentage of energy divided among the different magnetic field components. The resulting field is similar to that of TWA 25, with a dominantly toroidal field (34 per cent energy in poloidal components), and a very simple poloidal field with 90 per cent energy in dipolar and quadrupolar components. The poloidal field is also dominantly non-axisymmetric, with only 38 per cent for the poloidal field energy aligned with the rotation axis.

5 LONGITUDINAL MAGNETIC FIELD AND ACTIVITY INDICATORS

In addition to reconstructing the large-scale brightness and magnetic field morphologies, we explore other probes of stellar magnetic activity, namely the line-of-sight (longitudinal) magnetic field, B_l, and the H α and Na I doublet indices. These are plotted for both stars in Figs 10 and 11. The longitudinal magnetic field is calculated for each Stokes V profile using the program of Grunhut et al. (2013), which follows the method of Wade et al. (2000), using the mean Landé factor and mean wavelength of our Stokes V LSD profiles. Uncertainties in B_l are calculated by propagating the Stokes I and V LSD uncertainties. For TWA 7, we exclude incomplete observations (where only two of the four sub-exposures in the sequence were obtained), as without a full set of sub-exposures we are unable to calculate the null polarization profile needed to assess the level of spurious signal in our profiles.

We define an H α index following Marsden et al. (2014), using a rectangular emission bandpass of 0.36 nm, centred on 656.285 nm, and two continuum bandpasses in 0.22 nm, centred on 655.885 nm and 656.730 nm. For the Na I doublet indices, we define the index as in Gomes da Silva et al. (2011), with two rectangular emission bandpasses of width 0.1 nm centred on 589.592 and 588.995 nm, and two continuum bandpasses centred on 580.50 and 609.00 nm, with width 1.0 and 2.0 nm, respectively. All spectral indices are calculated in the stellar rest frame, with uncertainties calculated by propagation of the intensity spectra uncertainties. Figs 10 and 11 show B_l values plotted with 1σ error bars, and H α and Na I doublet indices are shown with 3σ error bars for clarity. The colours of the points represent the number of rotations, with purple being the first cycle, blue the second, green the third, and yellow the fourth observed cycle.
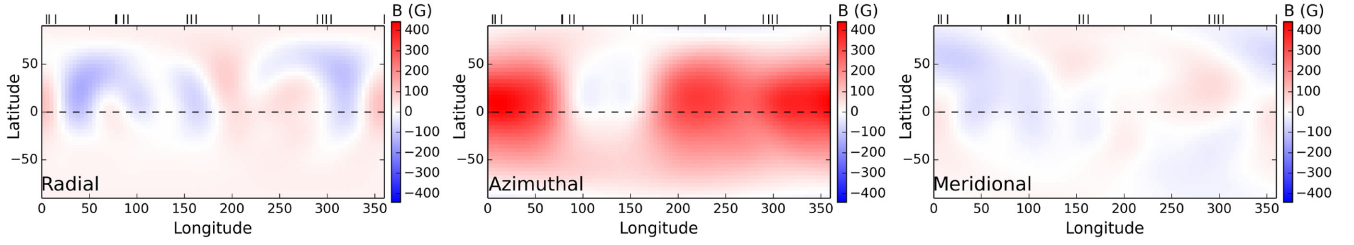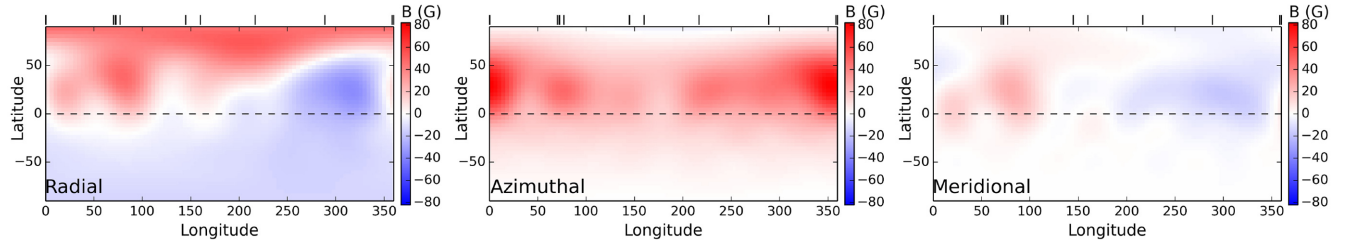
Figure 8. Large-scale radial (left), azimuthal (centre), and meridional (right) surface magnetic field maps of TWA 25 corresponding to the Stokes V fits in Fig. 2. These results a show strong azimuthal field compared to the radial and meridional field components. The poloidal (radial and meridional) field is simple and non-axisymmetric, with 80 per cent for the poloidal field energy contained in dipolar and quadrupolar components, and ∼97 per cent poloidal field energy in non-axisymmetric components.

Figure 9. The large-scale radial (left), azimuthal (centre), and meridional (right) surface magnetic field maps of TWA 7 corresponding to the Stokes V fits in Fig. 4. These results show a stronger azimuthal field than either the radial or meridional components. The poloidal (radial and meridional) field is quite simple with 90 per cent of the poloidal field energy in dipolar or quadrupolar components, and predominantly non-axisymmetry, with only 38 per cent of the poloidal field energy in axisymmetric components.
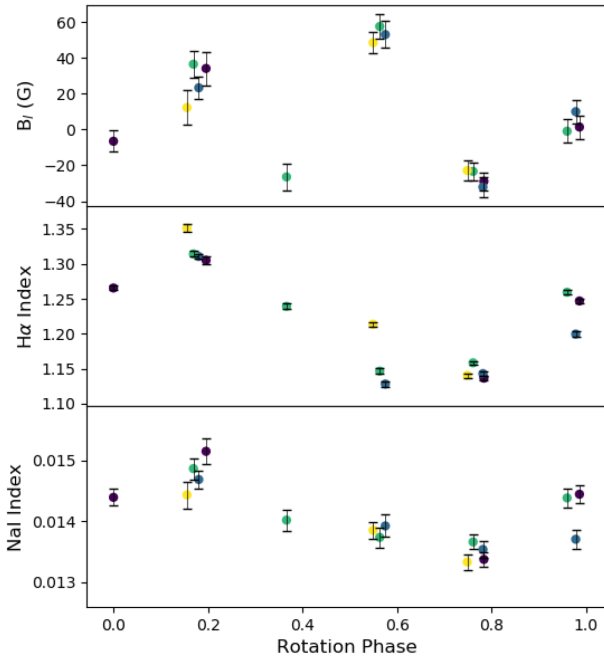
Figure 10. Plots of longitudinal magnetic field measurement (top), Hα indices (middle) and Na I doublet indices (bottom) for TWA 25. The colours of the points represent the number of rotations, with purple being the first cycle, blue the second, green the third, and yellow the fourth observed cycle.

Figure 11. Plots of longitudinal magnetic field measurement (top), H α indices (middle), and Na I doublet indices (bottom) for TWA 7. Colours are as per Fig. 10.

For both stars, we see a range of values in all activity measures, which is expected given the evolutionary states of these stars. TWA 25 shows variations in longitudinal magnetic field strengths, $|B_l|$, between 1 ± 7 G and 58 ± 7 G. Significant variation is also observed in the Hα indices, and to a lesser extent in the Na I doublet indices.
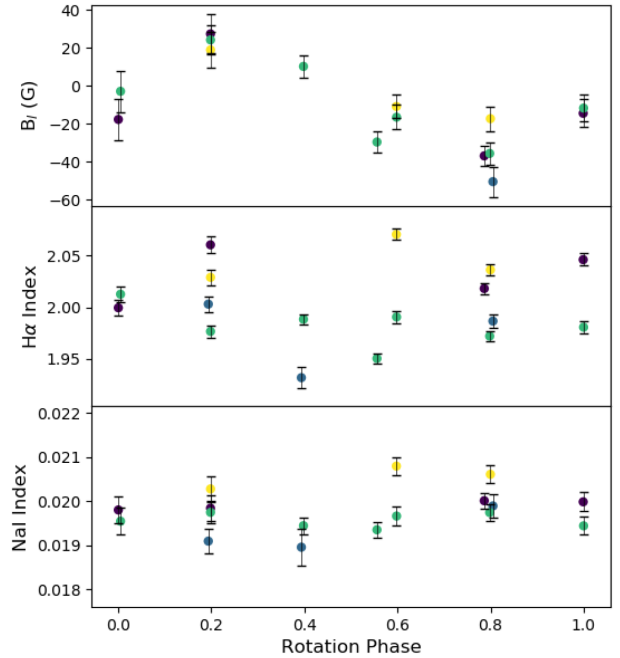
Across all observations of TWA 25, B_l measurements at a given observed phase have a small dispersion, indicating that the large-scale magnetic field is stable over the time span of our observations. This is also the case for the H α and Na I doublet indices, indicating that these changes are associated with particular features in the stellar
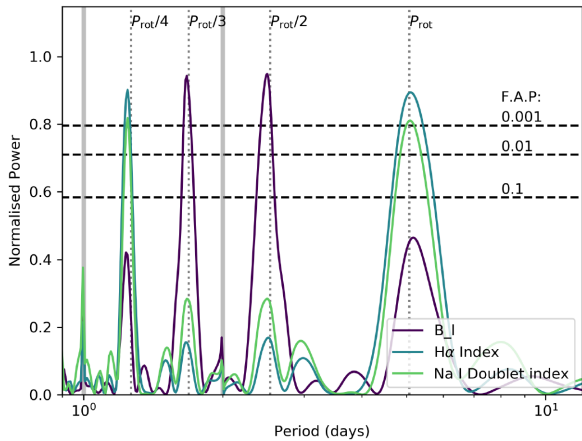
Figure 12. A generalized Lomb–Scargle periodogram of B_l, H α indices, and Na I Doublet indices for TWA 25.
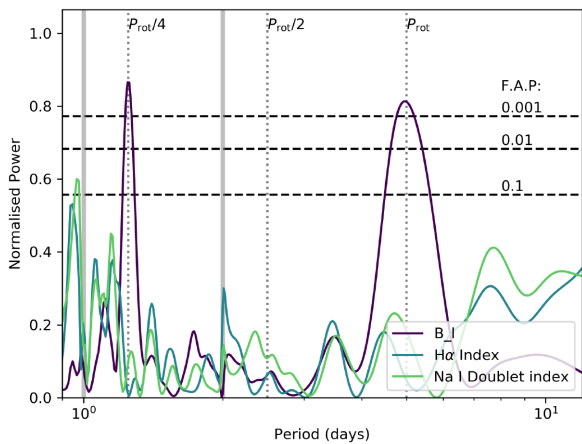

Figure 13. A generalized Lomb–Scargle periodogram of B_l, H α indices, and Na I Doublet indices for TWA 7.

surface, and that these features are also largely stable over the time span of our observations.

TWA 7 also displays variation in the longitudinal magnetic field, with $|B_l|$ values ranging between 3 ± 11 G and 50 ± 8 G. At a given observed phase, B_l values are consistent, indicating that the large-scale field is stable over the time span of our observations. The H α and Na I doublet indices, however, both display large dispersions at a given phase, with the first (purple points) and last (yellow points), showing systematically higher H α and Na I doublet index values than the other cycles. This indicates that the chromospheric active regions evolve more quickly than the large-scale photospheric magnetic field.

We analyse the periodicity of our B_l, H α, and Na I doublet indices for both stars with a Generalized Lomb Scargle periodogram (Zechmeister & Kürster 2009), using the PyAstronomy[2] package. These are shown in Fig. 12 for TWA 25 and in Fig. 13 for TWA 7. Included in these figures are vertical dotted lines, indicating the stellar rotation period and fractions of the rotation period, as well as horizontal dashed lines indicating the false alarm probability (FAP) levels. These FAP values are calculated in the PyAstronomy program as per equation (24) of Zechmeister & Kürster (2009). Both data sets are sampled approximately daily, giving an associated Nyquist

---

[2]https://github.com/sczesla/PyAstronomy

frequency of 0.5 d^{-1}. These are highlighted as grey lines at periods of 1 and 2 d, respectively.

The periodograms of B_l, H α, and Na I doublet indices for TWA 25 all show peaks around the stellar rotational period. For the H α and the Na I doublet, this is the second highest peak (the highest is around the one-fourth rotation period), but is still detectable above an FAP of 0.001. For the B_l values, however, the peak at the rotation period is small. Instead, the highest peak in B_l is at half the rotation period, with the second highest peak at one-third the rotation period. The dominance of these peaks at fractional aliases of the full rotation period reflects the magnetic field geometry: there are multiple magnetic regions that come into and out of the line of sight in a given rotation, giving signal power at fractions of that rotation period. All periodograms show a spike around the 1 d sampling rate, and small peaks at the 2 d period associated with the Nyquist frequency.

For TWA 7, the periodogram of B_l has the highest peak at one-fourth of the stellar rotation period with detectability at the FAP level of 0.001, and the second highest peak at the stellar rotation period. This is reflective of the dominantly dipolar and quadupolar field reconstructed, which shows multiple, regularly spaced magnetic regions, adding power at this fraction of the total rotation period. The H α and Na I doublet indices, however, do not have any peaks of significant power associated with the stellar rotation period. Instead, their highest peaks are around the cadence of observations of 1 d.

Taking the periodograms of both stars together shows that, while activity indices like Na I and H α can be useful in determining the stellar rotation period (e.g. TWA 25), this is not always the case (e.g. TWA 7), as also found by Hébrard et al. (2016). Thus, monitoring of the longitudinal magnetic field is an effective method of measuring stellar rotation, independent of the behaviour of the chromospheric activity indices.

6 RADIAL VELOCITIES

We analyse the radial velocities of TWA 25 by measuring the first order moment of each Stokes I profiles in the heliocentric rest frame, with uncertainties calculated as in Butler et al. (1996). These RV values are shown as pink diamonds in Fig. 14. We then use the fits from our surface brightness maps to filter out the activity-induced RV signal, by measuring the RVs of our DI fits (shown as an orange line in Fig. 14), and subtracting them from the radial velocities of our observations, as per the method of Donati et al. (2015). The resulting residuals are shown as purple circles in Fig. 14. In doing this, we reduce the RMS of the radial velocity variations from 465 to 42 m s^{-1}, which is of the same order as the mean uncertainty of 38 m s^{-1}. The semi-amplitude of the radial velocities is reduced from 833 to 81 m s^{-1}. The same radial velocity analysis was performed for TWA 7, and this is plotted in Fig. 15. The semi-amplitude of TWA7's radial velocities decreased from 191 to 68 m s^{-1}, and the RMS of the radial velocities was reduced from 127 to 36 m s^{-1}, below than the average uncertainty of 49 m s^{-1}.

The periodicity of the radial velocities and activity filtered residuals were analysed for both stars with a generalized Lomb–Scargle periodogram, using the same procedure as used for the activity indices. These are shown in Figs 16 and 17 for TWA 25 and TWA 7, respectively. The radial velocity periodograms for both stars show significant peaks at their rotation periods and the quarter harmonic of that period. The periodograms of the residual, activity filtered radial velocities have reduced power at those periods in both cases,
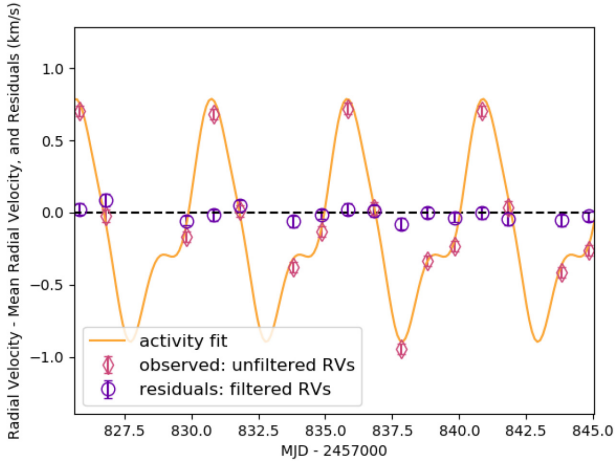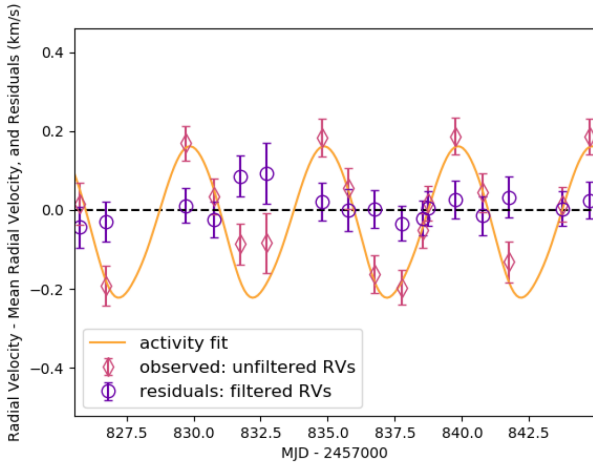
Figure 14. Radial velocities of TWA 25. The pink diamonds are the measured radial velocities of the LSD profiles (black lines in Fig. 1), the orange line is the radial velocity contribution from the surface brightness inhomogeneities, as measured from our fit to the surface brightness (red lines in Fig. 1), and the purple circles are the activity-filtered radial velocities, calculated by subtracting the brightness fit (orange line) from the measured radial velocity (pink diamonds). The RMS in the raw radial velocities is 465 m s^{-1}, which is further reduced to 42 m s^{-1} after filtering, of the same order as the mean uncertainty of 38 m s^{-1}.

Figure 15. Radial velocities of TWA 7. The pink diamonds are the measured radial velocities of the LSD profiles (black lines in Fig. 3), the orange line is the radial velocity contribution from the surface brightness inhomogeneities, as measured from our fits based on our surface brightness reconstruction (red lines in Fig. 3), and the purple circles are the activity filtered radial velocities, calculated by subtracting the brightness fit (orange line) from the measured radial velocity (pink diamonds). The RMS in the raw radial velocities is 127 m s^{-1}, which is reduced to 36 m s^{-1} after filtering, i.e. smaller than the mean error of 49 m s^{-1}.

but most notably in TWA 7, despite it being a challenging Doppler imaging target with a low $v\sin(i)$ and poorer signal-to-noise ratio.

Planet detection limits were determined for both stars based on the activity-filtered radial velocities by adding an artificial Keplerian signal to each data set, then performing an F-test to ask whether the two data sets (original and with added planetary signal) are significantly different at a 99 per cent confidence level. This approach has been used in cases where we have very limited data (usually $N <$ 40) and the traditional GLS periodogram recovery method becomes
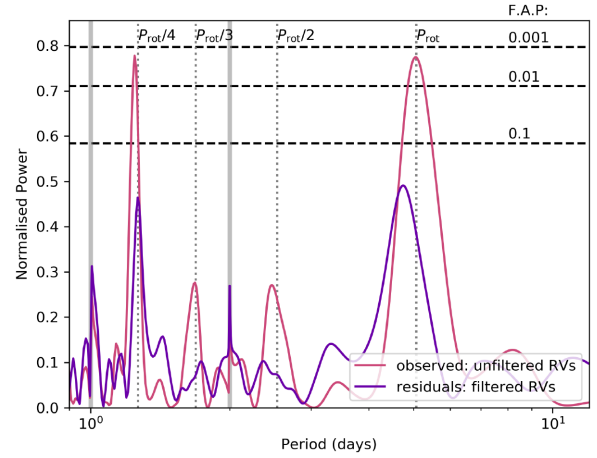
Figure 16. A generalized Lomb–Scargle periodogram of the radial velocities of TWA 25, and residuals after filtering for activity.
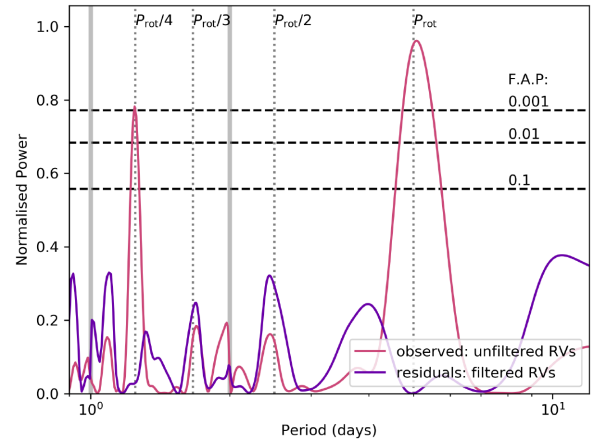

Figure 17. A generalized Lomb–Scargle periodogram of the radial velocities of TWA 7, and residuals after filtering for activity.

unreliable (Wittenmyer et al. 2020). This injection-recovery method is otherwise identical to that used in related exoplanet detection-efficiency studies (e.g. Wittenmyer et al. 2006, 2016; Wittenmyer & Marshall 2015). Given that the velocity data for both stars span only 19 days, we test orbital periods $P < 20$ days, corresponding to a maximum semimajor axis of $a \sim 0.13$ au. We further assume that close in planets would arrive there by disc migration, and so we test for circular orbits only. For each of the 20 trial orbital periods and 100 velocity semi-amplitudes K, we injected a circular Keplerian signal. For each (P, K) pair, we tested 1000 values of the orbital phase and performed an F-test comparing the original data with that to which the signal was added. The result is a recovery fraction for each (P, K) pair, as shown in Fig. 18. The spike seen in each data set occurs at an orbital period of 2 days, and so results from the sampling of our data and its associated Nyquist frequency of 0.5 d^{-1}. It should be stressed that since we perform these tests on the activity filtered data, we are insensitive to any signal around the rotation period of each star, as signals around those periods are removed through the filtering process. Aside from planets on those periods, in general, we can rule out planets at the 99 per cent confidence level with $M_p\sin i \gtrsim 1.0\ M_{\rm Jup}$ in close orbits around TWA 25, and $M_p\sin i \gtrsim 0.6\ M_{\rm Jup}$ for TWA 7. That is, our activity-corrected data permit the secure detection of close-in planets with $K \sim 100$ m s^{-1} for either star.
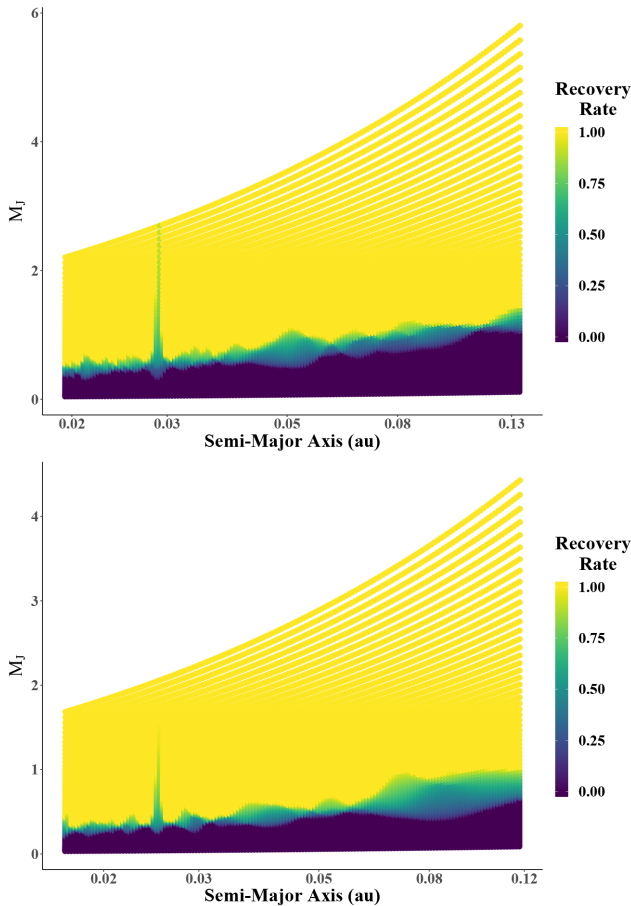
Figure 18. Detection probabilities for exoplanets orbiting TWA 25 (top panel), and TWA 7 (bottom panel), derived from the filtered RV data.

7 SUMMARY AND DISCUSSION

This paper presents the detailed analysis of high resolution spectropolarimetric data of 2 M-type wTTS, TWA 25 and TWA 7. Observations were taken between 2017 March 12–31, with a total of 16 observations for TWA 25, and 17 observations for TWA 7. Using Doppler imaging techniques, we reconstruct the large-scale surface brightness distributions for TWA 25 and TWA 7, and the large-scale magnetic fields for TWA 25 and TWA 7. In addition to this, we probe the stellar magnetic activity as a function of stellar rotation, by measuring the line-of-sight surface magnetic field, H α emission and core emission in the Na I doublet. We examine the radial velocity variations from both targets, and filter the stellar activity jitter from the radial velocity curves using our reconstructed brightness maps.

7.1 Dynamos in PMS stars

The magnetic field reconstructions for TWA 25 and TWA 7 add to the diversity of surface magnetic field morphologies found from spectropolarimetric studies of wTTS and in the wider PMS population. The strong toroidal fields reconstructed in TWA 25 and TWA 7 are similar to those seen in other wTTSs but differ significantly from CTTS with similar stellar properties. TWA 25 and TWA 7 are plotted in Fig. 19 alongside the rest of the WTTS (labelled and outlined in black), and the cTTS. WTTS display a larger range of magnetic field morphologies compared to cTTSs. While the large scale fields

of cTTS appear to show a dependence on the internal structure, the magnetic fields of wTTS display no such trends (Gregory et al. 2012).

These differences in the observed magnetic field behaviour of wTTS and cTTS suggest potential differences in the dynamos of accreting and non-accreting stars. It is interesting to note, however, that the dynamo models of Emeriau-Viard & Brun (2017) do not include accretion processes in their simulations, and yet produce results that are only consistent for the observed sample of accreting stars. Given wTTS overlap with the MaPP cTTSs in terms of their ages and stellar parameters, this sample is effectively also biased towards targets that have cleared their discs within approximately 10 Myr, and have like different initial conditions of formation. Simulations of magnetic field generation in low-mass stars report a 'bistability' in the dynamo simulations (Simitev & Busse 2009), where the resulting field configuration (either strong, poloidal and axisymmetric, or weak, toroidal, and non-axisymmetric) is sensitive to initial conditions, and a similar phenomenon may also explain the behaviour observed here.

The wider range in morphologies among the wTTSs compared to cTTSs could be explained by their wider range in rotation period. The rotation rates among cTTS are more homogeneous and are on average slower, as the coupling to the disc and processes that dissipate the angular momentum of the star mean that they do not reach the same rotation speeds as the wTTS that are not inhibited by these mechanisms as they contract and spin-up during transition towards the main sequence. There is a tentative relation among the classical T Tauri stars between rotation and morphology: the slower rotating cTTS are more likely to have large symmetric poloidal fields. However, we see wTTSs with similar rotation periods and vastly different magnetic field topologies, such as TWA 8A, TWA 7 and TWA 25 that all have rotation periods around ∼5 d, but have very different large-scale magnetic fields. TWA 8A has a large, dominantly poloidal and axisymmetric field, where as TWA 7 has a small, dominantly toroidal and non-axisymmetric field, and TWA 25 has the most Toroidal field of the T Tauri star sample. This suggests we cannot explain the variety in the scale fields in wTTS by the variety of their rotation periods.

Another possible explanation for the wide range in morphologies among the wTTS population is temporal variability. For the two stars presented in this paper, and recently all the other stars in the MaTYSSE sample are snapshot observations of these stars. Yu et al. (2019) have since published a series of 6 spectropolarimetric observations of V410 Tau between 2008 December and 2016 January.[3] Over these observations, V410 Tau varies in its degree of poloidal and toroidal field, and in the degree of axisymmetry, similar to but not as wide as the range of values observed across the whole wTTS population; TWA 25 is still the most toroidal least axisymmetric observed in the MaTYSSE sample. The observed mean magnetic field strength changes only marginally over the observations of V410 Tau, indicating that the observed differences in field strengths across the MaTYSSE wTTS sample are due to other phenomena.

We are unable to draw any definitive conclusions here, as the observed sample of T Tauri stars is still quite small. However, the advent of new infrared high-resolution spectropolarimeters, such as SpIRou on CFHT (Donati et al. 2020) and CRIRES+ on the ESO VLT (Follert et al. 2014), presents exciting opportunities in the study of T Tauri star magnetic fields, and particularly for the M-type stars in this class. These new instruments will provide useful insights

---

[3] An animated GIF depicting the variation of V410 Tau in the context of the updated TTS HR diagram can be found here: https://tinyurl.com/wcdjseps.
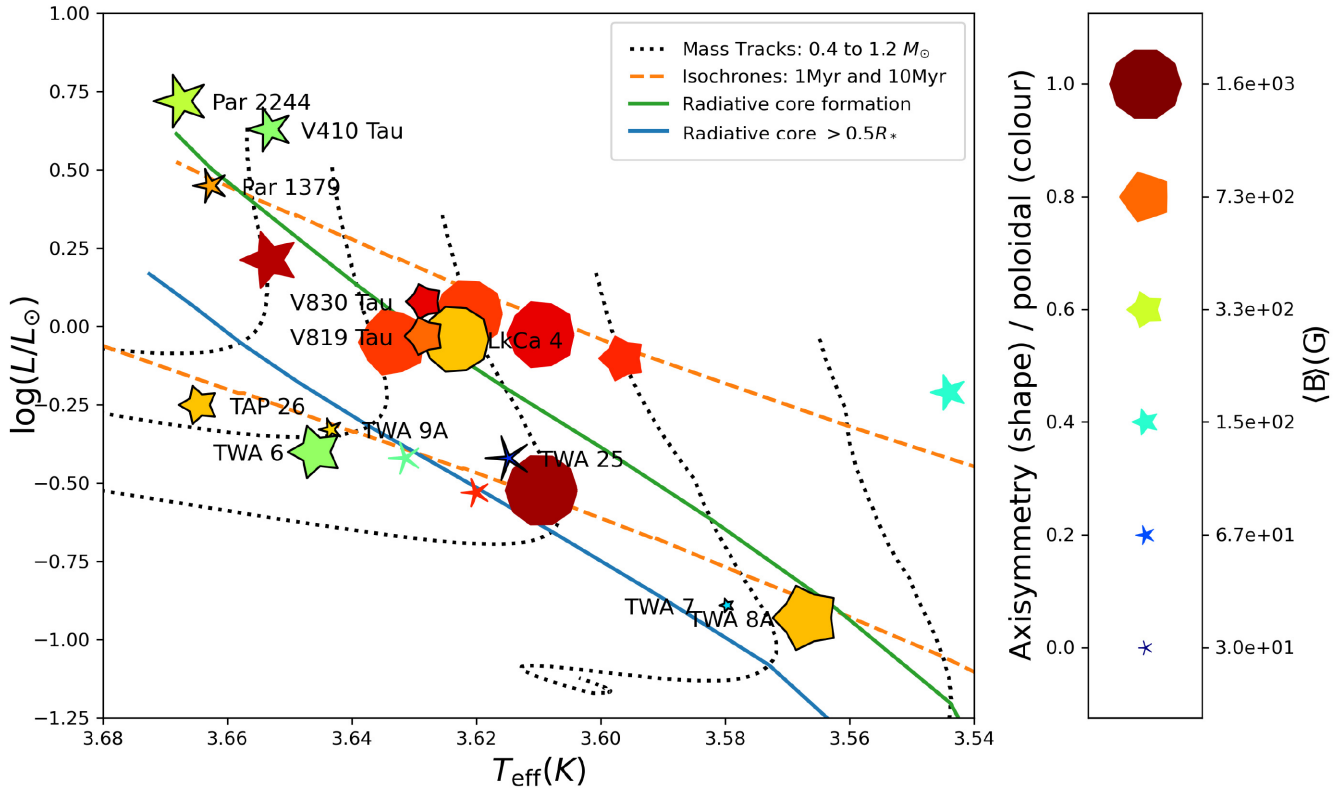
Figure 19. A Hertzsprung–Russell Diagram showing the updated MaTYSSE sample of WTTSs (outlined in black; additional data from Donati et al. 2014, 2015; Hill et al. 2017; Yu et al. 2017; Nicholson et al. 2018; Hill et al. 2019; Yu et al. 2019), and the MaPP sample of CTTSs (data from Donati et al. 2007, 2008; Donati et al. 2010; Donati et al. 2010, 2011; Donati et al. 2011, 2012, 2013). The size of each point represents the mean magnetic field strength, the colour indicates the percentage of magnetic field energy in poloidal components, and the shape indicates the percentage of poloidal field energy in axisymmetric components. The point for V410 Tau uses the mean of the six observations made by Yu et al. (2019). The black dotted lines show the (right to left) 0.4, 0.6, 0.8, 1.0, and 1.2 $M_\odot$ mass tracks from the Baraffe et al. (2015) PMS evolution models, as well as 1 Myr (top) and 10 Myr (bottom) isochrones as orange dashed lines. The boundary in evolution where a radiative core begins to form in indicated by the solid green line, and where the radiative core becomes greater than half the radius of the star is given by the solid blue line.

into these cooler stars in greater numbers than is possible at optical wavelengths, allowing us to build statistically significant samples and also to further explore temporal variability in the large-scale magnetic fields of PMS stars.

7.2 Radial velocities and stellar activity

Both TWA 25 and TWA 7 exhibit large, periodic variations in their radial velocities. In both stars, the surface spot and plage regions create large distortions in the spectral absorption line, which we are able to characterise with DI, and filter their contribution to the RV variability. For TWA 25, we reduce the RMS of our RVs from 465 to 42 m s^{-1}, which is in line with our mean uncertainty of 38 m s^{-1}, and for TWA 7 reduce the RMS from 127 to 36 m s^{-1}, less than the average uncertainty of 49 m s^{-1}. Given the amplitude of these filtered radial velocities, the period and sampling of observations, and the uncertainties on our radial velocity measurements, for TWA 25 we can rule out a planet with $M_p \sin i$ greater than 1.0 Jupiter masses, orbiting closer than 0.13 au, and for TWA 7 we can rule out a planet with $M_p \sin i$ greater than 0.6 Jupiter masses, orbiting closer than 0.13 au. We thus exclude the presence of close in giant planets for both of these stars.

TWA 7 is an example of a 'false positive' planet signal in the radial velocities of an active star. It shows large, sinusoidal radial velocity variations without obvious line distortion, as is typical

for stars at these inclinations. At face value it is easy to assume that such a motion could be caused by a planet, and the lack of periodicity in activity indices and small amplitudes in line bisectors compared with the RV amplitude supports this. However, given the variability in our circularly polarized spectra, which trace the variations in longitudinal magnetic field, we can infer that this radial velocity signal is likely caused by stellar activity. It is reminiscent of the case of TWA Hya, where a hot Jupiter was hypothezised to be orbiting on the same period as the stellar rotation period (Setiawan et al. 2008), but this signal was later shown to be caused by a dark surface feature (Donati et al. 2011). This study further highlights the usefulness of longitudinal magnetic field measurements for indicating the stellar activity origins of radial velocity variations, where traditional chromospheric activity indices might fail.

Given the lack of exoplanet detections for both stars, we can adjust the observed occurrence rate of hot Jupiters around wTTSs from 1 in 5 to 1 in 6, as measured by the MaTYSSE sample (2 detections within the now total sample of 12). This is still dramatically higher than the MS occurrence rate of 1 per cent, but the MaTYSSE sample is still very small, and a larger sample is needed to estimate the true occurrence rate. The new generation of high-resolution spectropolarimeters-mentioned above will help greatly with establishing more robust statistics of hot Neptunes and Jupiters around young stars.

ACKNOWLEDGEMENTS

DATA AVAILABILITY

The data underlying this article can be accessed from the European Southern Observatory Science Archive. The derived data generated in this research will be shared on reasonable request to the corresponding author.

REFERENCES

Alvarado-Gómez J. D. et al., 2015, A&A, 582, A38
Ammons S. M., Robinson S. E., Strader J., Laughlin G., Fischer D., Wolf A., 2006, ApJ, 638, 1004
Baraffe I., Homeier D., Allard F., Chabrier G., 2015, A&A, 577, A42
Butler R. P., Marcy G. W., Williams E., McCarthy C., Dosanjh P., Vogt S. S., 1996, PASP, 108, 500
Choquet É. et al., 2016, ApJ, 817, L2
Collier Cameron A., 1997, MNRAS, 287, 556
da Silva L., Torres C. A. O., de La Reza R., Quast G. R., Melo C. H. F., Sterzik M. F., 2009, A&A, 508, 833
Donati J. F., Semel M., Carter B. D., Rees D. E., Collier Cameron A., 1997, MNRAS, 291, 658
Donati J. F., Wade G. A., Babel J., Henrichs H. F., de Jong J. A., Harries T. J., 2001, MNRAS, 326, 1265
Donati J. F. et al., 2010, MNRAS, 402, 1426
Donati J. F. et al., 2011, MNRAS, 417, 472
Donati J. F. et al., 2013, MNRAS, 436, 881
Donati J. F. et al., 2014, MNRAS, 444, 3220
Donati J. F. et al., 2015, MNRAS, 453, 3706
Donati J. F. et al., 2020, MNRAS, 498, 5684
Donati J.-F. et al., 2007, MNRAS, 380, 1297
Donati J.-F. et al., 2008, MNRAS, 386, 1234
Donati J.-F. et al., 2010, MNRAS, 409, 1347
Donati J.-F. et al., 2011, MNRAS, 417, 1747
Donati J.-F. et al., 2012, MNRAS, 425, 2948
Emeriau-Viard C., Brun A. S., 2017, ApJ, 846, 8
Follert R. et al., 2014, in Ramsay S. K., McLean I. S., Takami H., eds, Proc. SPIE, Vol. 9147, Ground-based and Air- borne Instrumentation for Astronomy V. SPIE, Bellingham, p. 914719
Folsom C. P. et al., 2018, MNRAS, 474, 4956
Gaia Collaboration et al., 2016, A&A, 595, A1
Gaia Collaborationet al., 2018, A&A, 616, A1
Gomes da Silva J., Santos N. C., Bonfils X., Delfosse X., Forveille T., Udry S., 2011, A&A, 534, A30
Gregory S. G., Donati J.-F., Morin J., Hussain G. A. J., Mayne N. J., Hillenbrand L. A., Jardine M., 2012, ApJ, 755, 97
Grunhut J. H. et al., 2013, MNRAS, 428, 1686
Gully-Santiago M. A. et al., 2017, ApJ, 836, 200
Hébrard É. M., Donati J. F., Delfosse X., Morin J., Moutou C., Boisse I., 2016, MNRAS, 461, 1465
Henden A. A., Templeton M., Terrell D., Smith T. C., Levine S., Welch D., 2015, Am. Astron. Soc. Meeting Abstr., 225, 336.16
Hill C. A., Carmona A., Donati J. F., Hussain G. A. J., Gregory S. G., Alencar S. H. P., Bouvier J., The Matysse Collaboration, 2017, MNRAS, 472, 1716
Hill C. A., Folsom C. P., Donati J. F., Herczeg G. J., Hussain G. A. J., Alencar S. H. P., Gregory S. G., Matysse Collaboration, 2019, MNRAS, 484, 5810
Hussain G. A. J., Donati J.-F., Collier Cameron A., Barnes J. R., 2000, MNRAS, 318, 961
Hussain G. A. J., van Ballegooijen A. A., Jardine M., Collier Cameron A., 2002, ApJ, 575, 1078
Hussain G. A. J. et al., 2009, MNRAS, 398, 189
Hussain G. A. J. et al., 2016, A&A, 585, A77
Low F. J., Smith P. S., Werner M., Chen C., Krause V., Jura M., Hines D. C., 2005, ApJ, 631, 1170
Marsden S. C. et al., 2014, MNRAS, 444, 3517
McDonald I., Zijlstra A. A., Watson R. A., 2017, MNRAS, 471, 770
Mentuch E., Brandeker A., van Kerkwijk M., Jayawardhana R., Hauschildt P., 2008, ApJ, 689, 1127
Nicholson B. A., Hussain G. A. J., Donati J.-F., Folsom C. P., Mengel M., Carter B. D., Wright D., 2018, MNRAS, 480, 1754
Olofsson J., et al. 2018, A&A, 617, A109
Pecaut M. J., Mamajek E. E., 2013, ApJS, 208, 9
Ryabchikova T., Piskunov N., Kurucz R. L., Stempels H. C., Heiter U., Pakhomov Y., Barklem P. S., 2015, Phys. Scr., 90, 054005
Setiawan J., Henning T., Launhardt R., Müller A., Weise P., Kürster M., 2008, Nature, 451, 38
Siess L., Dufour E., Forestini M., 2000, A&A, 358, 593
Simitev R. D., Busse F. H., 2009, EPL (Eur. Lett.), 85, 19001
Song I., Zuckerman B., Bessell M. S., 2003, ApJ, 599, 342
Valenti J. A., Fischer D. A., 2005, ApJS, 159, 141
Wade G. A., Donati J. F., Landstreet J. D., Shorlin S. L. S., 2000, MNRAS, 313, 851
Webb R. A., Zuckerman B., Platais I., Patience J., White R. J., Schwartz M. J., McCarthy C., 1999, ApJ, 512, L63
Wittenmyer R. A., Marshall J. P., 2015, AJ, 149, 86
Wittenmyer R. A., Endl M., Cochran W. D., Hatzes A. P., Walker G. A. H., Yang S. L. S., Paulson D. B., 2006, AJ, 132, 177
Wittenmyer R. A. et al., 2016, ApJ, 819, 28
Wittenmyer R. A. et al., 2020, MNRAS, 491, 5248
Yang H., Johns-Krull C. M., Valenti J. A., 2008, AJ, 136, 2286
Yu L. et al., 2017, MNRAS, 467, 1342
Yu L. et al., 2019, MNRAS, 489, 5556
Zechmeister M., Kürster M., 2009, A&A, 496, 577

This paper has been typeset from a TEX/LATEX file prepared by the author.

List of astronomical key words (Updated on 2020 January)

This list is common to *Monthly Notices of the Royal Astronomical Society, Astronomy and Astrophysics*, and *The Astrophysical Journal*. In order to ease the search, the key words are subdivided into broad categories. No more than *six* subcategories altogether should be listed for a paper.

The subcategories in boldface containing the word 'individual' are intended for use with specific astronomical objects; these should never be used alone, but always in combination with the most common names for the astronomical objects in question. Note that each object counts as one subcategory within the allowed limit of six.

The parts of the key words in italics are for reference only and should be omitted when the keywords are entered on the manuscript.

General
editorials, notices
errata, addenda
extraterrestrial intelligence
history and philosophy of astronomy
miscellaneous
obituaries, biographies
publications, bibliography
sociology of astronomy
standards

Physical data and processes
acceleration of particles
accretion, accretion discs
asteroseismology
astrobiology
astrochemistry
astroparticle physics
atomic data
atomic processes
black hole physics
chaos
conduction
convection
dense matter
diffusion
dynamo
elementary particles
equation of state
gravitation
gravitational lensing: micro
gravitational lensing: strong
gravitational lensing: weak
gravitational waves
hydrodynamics
instabilities
line: formation
line: identification
line: profiles
magnetic fields
magnetic reconnection
(magnetohydrodynamics) MHD
masers
molecular data
molecular processes
neutrinos
nuclear reactions, nucleosynthesis, abundances
opacity
plasmas
polarization

radiation: dynamics
radiation mechanisms:general
radiation mechanisms: non-thermal
radiation mechanisms: thermal
radiative transfer
relativistic processes
scattering
shock waves
solid state: refractory
solid state: volatile
turbulence
waves

Astronomical instrumentation, methods and techniques
atmospheric effects
balloons
instrumentation: adaptive optics
instrumentation: detectors
instrumentation: high angular resolution
instrumentation: interferometers
instrumentation: miscellaneous
instrumentation: photometers
instrumentation: polarimeters
instrumentation: spectrographs
light pollution
methods: analytical
methods: data analysis
methods: laboratory: atomic
methods: laboratory: molecular
methods: laboratory: solid state
methods: miscellaneous
methods: numerical
methods: observational
methods: statistical
site testing
space vehicles
space vehicles: instruments
techniques: high angular resolution
techniques: image processing
techniques: imaging spectroscopy
techniques: interferometric
techniques: miscellaneous
techniques: photometric
techniques: polarimetric
techniques: radar astronomy
techniques: radial velocities
techniques: spectroscopic
telescopes

Astronomical data bases
astronomical data bases: miscellaneous
atlases
catalogues
surveys
virtual observatory tools

Software
software: data analysis
software: development
software: documentation
software: public release
software: simulations

Astrometry and celestial mechanics
astrometry
celestial mechanics
eclipses
ephemerides
occultations
parallaxes
proper motions
reference systems
time

The Sun
Sun: abundances
Sun: activity
Sun: atmosphere
Sun: chromosphere
Sun: corona
Sun: coronal mass ejections (CMEs)
Sun: evolution
Sun: faculae, plages
Sun: filaments, prominences
Sun: flares
Sun: fundamental parameters
Sun: general
Sun: granulation
Sun: helioseismology
Sun: heliosphere
Sun: infrared
Sun: interior
Sun: magnetic fields
Sun: oscillations
Sun: particle emission
Sun: photosphere
Sun: radio radiation
Sun: rotation
(Sun:) solar–terrestrial relations
(Sun:) solar wind
(Sun:) sunspots
Sun: transition region
Sun: UV radiation
Sun: X-rays, gamma-rays

Planetary systems
comets: general

comets: individual: . . .
Earth
interplanetary medium
Kuiper belt: general

Kuiper belt objects: individual: . . .
meteorites, meteors, meteoroids

minor planets, asteroids: general
minor planets, asteroids: individual: . . .
Moon
Oort Cloud
planets and satellites: atmospheres
planets and satellites: aurorae
planets and satellites: composition
planets and satellites: detection
planets and satellites: dynamical evolution and stability
planets and satellites: formation
planets and satellites: fundamental parameters
planets and satellites: gaseous planets
planets and satellites: general

planets and satellites: individual: . . .
planets and satellites: interiors
planets and satellites: magnetic fields
planets and satellites: oceans
planets and satellites: physical evolution
planets and satellites: rings
planets and satellites: surfaces
planets and satellites: tectonics
planets and satellites: terrestrial planets
planet–disc interactions
planet–star interactions
protoplanetary discs
zodiacal dust

Stars
stars: abundances
stars: activity
stars: AGB and post-AGB
stars: atmospheres
(stars:) binaries *(including multiple)*: close
(stars:) binaries: eclipsing
(stars:) binaries: general
(stars:) binaries: spectroscopic
(stars:) binaries: symbiotic
(stars:) binaries: visual
stars: black holes
(stars:) blue stragglers
(stars:) brown dwarfs
stars: carbon
stars: chemically peculiar
stars: chromospheres
(stars:) circumstellar matter
stars: coronae
stars: distances
stars: dwarf novae
stars: early-type
stars: emission-line, Be
stars: evolution
stars: flare
stars: formation
stars: fundamental parameters
(stars:) gamma-ray burst: general
(stars:) **gamma-ray burst: individual: . . .**
stars: general
(stars:) Hertzsprung–Russell and colour–magnitude diagrams
stars: horizontal branch
stars: imaging
stars: individual: . . .
stars: interiors

stars: jets
stars: kinematics and dynamics
stars: late-type
stars: low-mass
stars: luminosity function, mass function
stars: magnetars
stars: magnetic field
stars: massive
stars: mass-loss
stars: neutron
(stars:) novae, cataclysmic variables
stars: oscillations *(including pulsations)*
stars: peculiar *(except chemically peculiar)*
(stars:) planetary systems
stars: Population II
stars: Population III
stars: pre-main-sequence
stars: protostars
(stars:) pulsars: general
(stars:) **pulsars: individual: . . .**
stars: rotation
stars: solar-type
(stars:) starspots
stars: statistics
(stars:) subdwarfs
(stars:) supergiants
(stars:) supernovae: general
(stars:) **supernovae: individual: . . .**
stars: variables: Cepheids
stars: variables: Scuti
stars: variables: general
stars: variables: RR Lyrae
stars: variables: S Doradus
stars: variables: T Tauri, Herbig Ae/Be
(stars:) white dwarfs
stars: winds, outflows
stars: Wolf–Rayet

Interstellar medium (ISM), nebulae
ISM: abundances
ISM: atoms
ISM: bubbles
ISM: clouds
(ISM:) cosmic rays
(ISM:) dust, extinction
ISM: evolution
ISM: general
(ISM:) HII regions
(ISM:) Herbig–Haro objects

ISM: individual objects: . . .
(except planetary nebulae)
ISM: jets and outflows
ISM: kinematics and dynamics
ISM: lines and bands
ISM: magnetic fields
ISM: molecules
(ISM:) photodissociation region (PDR)
(ISM:) planetary nebulae: general
(ISM:) **planetary nebulae: individual: . . .**
ISM: structure
ISM: supernova remnants

The Galaxy
Galaxy: abundances
Galaxy: bulge
Galaxy: centre
Galaxy: disc
Galaxy: evolution
Galaxy: formation
Galaxy: fundamental parameters
Galaxy: general
(Galaxy:) globular clusters: general
(Galaxy:) **globular clusters: individual: . . .**
Galaxy: halo
Galaxy: kinematics and dynamics
(Galaxy:) local interstellar matter
Galaxy: nucleus
(Galaxy:) open clusters and associations: general
(Galaxy:) **open clusters and associations: individual: . . .**
(Galaxy:) solar neighbourhood
Galaxy: stellar content
Galaxy: structure

Galaxies
galaxies: abundances
galaxies: active
galaxies: bar
(galaxies:) BL Lacertae objects: general
(galaxies:) **BL Lacertae objects: individual: . . .**
galaxies: bulges
galaxies: clusters: general

galaxies: clusters: individual: . . .
galaxies: clusters: intracluster medium
galaxies: disc
galaxies: distances and redshifts
galaxies: dwarf
galaxies: elliptical and lenticular, cD
galaxies: evolution
galaxies: formation
galaxies: fundamental parameters
galaxies: general
galaxies: groups: general

galaxies: groups: individual: . . .
galaxies: haloes
galaxies: high-redshift

galaxies: individual: . . .
galaxies: interactions
(galaxies:) intergalactic medium
galaxies: irregular
galaxies: ISM
galaxies: jets
galaxies: kinematics and dynamics
(galaxies:) Local Group
galaxies: luminosity function, mass function
(galaxies:) Magellanic Clouds
galaxies: magnetic fields
galaxies: nuclei
galaxies: peculiar
galaxies: photometry
(galaxies:) quasars: absorption lines
(galaxies:) quasars: emission lines
(galaxies:) quasars: general

(galaxies:) **quasars: individual: . . .**
(galaxies:) quasars: supermassive black holes
galaxies: Seyfert
galaxies: spiral
galaxies: starburst
galaxies: star clusters: general

galaxies: star clusters: individual: . . .
galaxies: star formation
galaxies: statistics
galaxies: stellar content
galaxies: structure

Cosmology
(cosmology:) cosmic background radiation
(cosmology:) cosmological parameters
(cosmology:) dark ages, reionization, first stars
(cosmology:) dark energy
(cosmology:) dark matter
(cosmology:) diffuse radiation
(cosmology:) distance scale
(cosmology:) early Universe
(cosmology:) inflation
(cosmology:) large-scale structure of Universe
cosmology: miscellaneous
cosmology: observations
(cosmology:) primordial nucleosynthesis
cosmology: theory

Resolved and unresolved sources as a function of wavelength
gamma-rays: diffuse background
gamma-rays: galaxies
gamma-rays: galaxies: clusters
gamma-rays: general
gamma-rays: ISM
gamma-rays: stars
infrared: diffuse background
infrared: galaxies
infrared: general
infrared: ISM
infrared: planetary systems
infrared: stars
radio continuum: galaxies
radio continuum: general
radio continuum: ISM
radio continuum: planetary systems
radio continuum: stars
radio continuum: transients
radio lines: galaxies
radio lines: general
radio lines: ISM
radio lines: planetary systems
radio lines: stars
submillimetre: diffuse background
submillimetre: galaxies
submillimetre: general
submillimetre: ISM
submillimetre: planetary systems
submillimetre: stars
ultraviolet: galaxies

ultraviolet: general
ultraviolet: ISM
ultraviolet: planetary systems
ultraviolet: stars
X-rays: binaries
X-rays: bursts
X-rays: diffuse background
X-rays: galaxies
X-rays: galaxies: clusters
X-rays: general
X-rays: individual: . . .
X-rays: ISM
X-rays: stars

Transients
(transients:) black hole mergers
(transients:) black hole - neutron star mergers
(transients:) fast radio bursts
(transients:) gamma-ray bursts
(transients:) neutron star mergers
transients: novae
transients: supernovae
transients: tidal disruption events